FRONTIERS OF PHYSICS

RESEARCH ARTICLE
Volume 19 / Issue 6 / 63206 / 2024

Giant anomalous transverse transport properties of Co-doped two-dimensional Fe_3GaTe_2

Imran Khan, Jisang Hong†

Department of Physics, Pukyong National University, Busan 48513, Republic of Korea
Corresponding author. E-mail: †hongj@pknu.ac.kr
Received February 4, 2024; accepted May 25, 2024

ABSTRACT

In spintronics, transverse anomalous transport properties have emerged as a highly promising avenue surpassing the conventional longitudinal transport behaviors. Here, we explore the transverse transport properties of monolayer and bilayer $Fe_{3-x}Co_xGaTe_2$ (x = 0.083, 0.167, 0.250, and 0.330) systems. All the systems exhibit ferromagnetic ground states with metallic features and also have perpendicular magnetic anisotropy. Besides, the magnetic anisotropy is substantially enhanced with increasing Co-doping concentration. However, unlike magnetic anisotropy, the Curie temperature is suppressed by increasing the Co-doping concentration. For instance, the monolayer and bilayer $Fe_{2.917}Co_{0.083}GaTe_2$ hold a Curie temperature of 253 K and 269 K, which decreases to 163 K and 173 K in monolayer and bilayer $Fe_{2.67}Co_{0.33}GaTe_2$ systems, respectively. We find a giant anomalous Nernst conductivity (ANC) of 6.03 A/(K·m) in the monolayer $Fe_{2.917}Co_{0.083}GaTe_2$ at –30 meV, and this is further enhanced to 11.30 A/(K·m) in the bilayer $Fe_{2.917}Co_{0.083}GaTe_2$ at –20 meV. Moreover, the bilayer $Fe_{2.917}Co_{0.083}GaTe_2$ structure has a large anomalous thermal Hall conductivity (ATHC) of –0.14 W/(K·m) at 100 K. Overall, we find that the $Fe_{3-x}Co_xGaTe_2$ (x = 0.083, 0.167, 0.250, and 0.330) structures have better anomalous transverse transport performance than the pristine Fe_3GaTe_2 system and can be used for potential spintronics and spin caloritronics applications.

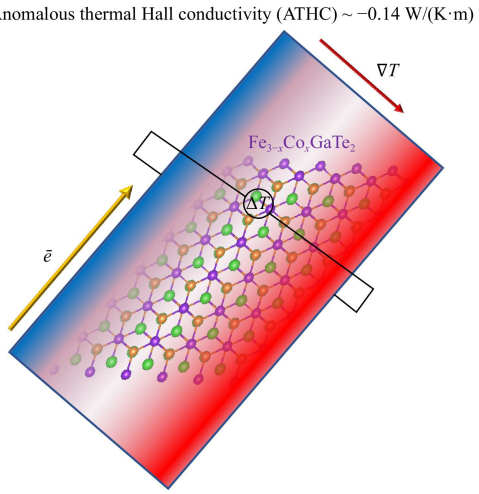

Keywords two-dimensional (2D) material, Fe_3GaTe_2, ferromagnetism, magnetic anisotropy, Curie temperature, anomalous Hall conductivity, anomalous Nernst conductivity, anomalous thermal Hall conductivity

1 Introduction

Introducing ferromagnetism in two-dimensional (2D) materials through some external agencies, such as introducing defects [1, 2], doping [3], or making edges [1, 4] has been widely studied in the past. However, the ferromagnetism created in this way does not have long-range ordering. Thanks to the advancement in exfoliation and measurement techniques, it is possible to exfoliate van der Waals (vdW) layered magnetic materials from a few layers down to even monolayer limits and measure their magnetic properties experimentally [5, 6]. Similarly, with the development of growth techniques, it becomes possible to control the growth of atomically thin layers [7, 8]. These developments have brought extensive research interest in 2D magnetic materials. The real breakthrough started with the discovery of layer-dependent ferromagnetism in the monolayer CrI_3 and bilayer $Cr_2Ge_2Te_6$ [9,

Higher Education Press

https://doi.org/10.1007/s11467-024-1424-5

10]. However, these materials possess relatively low Curie temperatures ~45 Kelvin (K). In this same family of the CrI_3 structure, monolayer $CrCl_3$, and $CrBr_3$ are also ferromagnetic semiconductors but with low Curie temperatures of ~17 K and ~31 K [11]. $CrSe_2$ is another experimentally synthesized material with metallic ferromagnetic (FM) order. This $CrSe_2$ shows a Curie temperature of 110 K in a 16-layer thick film. However, the Curie temperature decreases to 65 K in the monolayer thickness on the WSe_2 substrate [12]. For spintronics device applications, it is necessary to find a material that possesses a room-temperature ferromagnetism. In this aspect, Fe_3GeTe_2 has attracted extensive research interest because the bulk Fe_3GeTe_2 exhibited FM order with large out-of-plane magnetocrystalline anisotropy and a Curie temperature of ~220 K. It was also reported that the Curie temperature of 2D Fe_3GeTe_2 (130 K) could be enhanced to 230 K, and ~300 K through Fe-intercalation and ionic gating approach [13–15]. Recently, Fe_3GaTe_2 was also successfully synthesized down to a thickness of ~9.5 nm. A large Curie temperature of ~380 K and out-of-plane anisotropy were reported in the Fe_3GaTe_2 thin film [16].

Transport properties of magnetic materials play an important role in diverse spintronics applications and are widely studied on both experimental and theoretical sides. In the transport properties of magnetic materials, it is advantageous to utilize the transverse transport properties such as anomalous Hall conductivity (AHC), anomalous Nernst conductivity (ANC), and anomalous thermal Hall conductivity (ATHC) than the longitudinal transport properties [17, 18]. A key quantity among these transverse transport properties is the AHC because all the transverse transport properties are correlated to this AHC. The intrinsic AHC can be computed as a sum of the Berry curvature of the Bloch wave function over the occupied electronic states [19–21]. Extensive studies have been performed on the transport properties of bulk-type or 2D materials. For instance, layer-dependent ferromagnetism and intrinsic AHC were reported in 2D Fe_3GeTe_2 film down to the monolayer limit [22]. Besides, the strain-dependent room temperature ferromagnetism and AHC of ~400 S/cm was also found in monolayer $Cr_2Ge_2Se_6$ and $Cr_2Ge_2Te_6$ [23]. Furthermore, carrier-doping-induced ANC of –6.65 μV/K at 100 K was also theoretically reported in the $FeCl_2$ monolayer [24]. In addition, a large ANC of –14 A/(K·m) at 300 K was reported in the Co_2FeAl thin film of thickness ~10 nm, while the Co_2MnSi had a small ANC of 0.28 A/(K·m) at 300 K [25]. In a recent experimental study, an AHC of ~73 S/cm was reported in the Fe_3GaTe_3 thin film with a thickness of around 178 nm at 3 K. Note that the AHC of this relatively thick Fe_3GaTe_3 film shows a decreasing trend with increasing temperature [16]. Recently, we also calculated the thickness-dependent AHC of the Fe_3GaTe_2 in the thickness range from monolayer to four layers. A large AHC of around –490 S/cm was found in a four-layer Fe_3GaTe_2 system [26]. This implies that the AHC displays strong thickness-dependent characteristics. Since the experimental study shows that the magnetic properties of the Fe_5GeTe_2 flakes can be tuned by Co doping [27], we expect that the transverse transport properties of the Fe_3GaTe_2 system can also be affected by Co doping. Thus, in this report, we aim to systematically explore the anomalous transverse transport properties of Co doped Fe_3GaTe_2 by changing the Co doping concentration in both monolayer and bilayer structures, $Fe_{3-x}Co_xGaTe_2$ (x = 0.083, 0.167, 0.250, and 0.330) systems. Herein, we will propose that the anomalous transverse transport properties can be substantially enhanced in atomically thin bilayer $Fe_{3-x}Co_xGaTe_2$ layer systems compared with that found in the pristine four-layer Fe_3GaTe_2 system.

2 Numerical method

The concentration-dependent structural, electronic, and magnetic properties of monolayer and bilayer Co-doped $Fe_{3-x}Co_xGaTe_2$ systems are investigated using the Vienna ab initio simulation package (VASP) [28, 29]. We consider four different doping concentrations; for instance, x = 0.083, 0.167, 0.250, and 0.330 in monolayer and bilayer $Fe_{3-x}Co_xGaTe_2$ systems. We apply the generalized gradient approximation of Perdew–Burke–Ernzerhof (PBE) as exchange and correlation functional [30]. A slab geometry with a vacuum distance of more than 12 Å in the z-direction is applied to simulate all the layered structures. The structures are fully optimized after Co-doping without any constraints using the conjugate gradient method. A plane-wave basis set with an energy cutoff of 650 eV is used and the force and energy convergence criteria are set to 0.02 eV/Å and 10^{-6} eV for all the calculations. A Γ-centered k-points mesh of 11 × 11 × 1 is used for structure relaxation and electronic calculations. Furthermore, due to the weak van der Waals interaction between layers, we include the dispersion correction using the DFT-D3 method with Becke–Johnson damping function [31, 32]. To calculate the magnetocrystalline anisotropy energy (MAE), we utilize a non-collinear total energy method including the spin–orbit coupling (SOC) [33]. The MAE is determined by calculating the total energy difference between in-plane [001] and out-of-plane [100] magnetization directions. For these calculations, we employ a denser k-mesh of 15 × 15 × 1. The Metropolis Monte Carlo (MC) simulations are used to calculate the Curie temperature (T_C) [34, 35]. Furthermore, the Wannier interpolation technique is used to obtain the intrinsic Berry curvature contribution to the anomalous Hall conductivity (AHC). The Wannier functions are extracted from band structures using the maximally localized Wannier function method

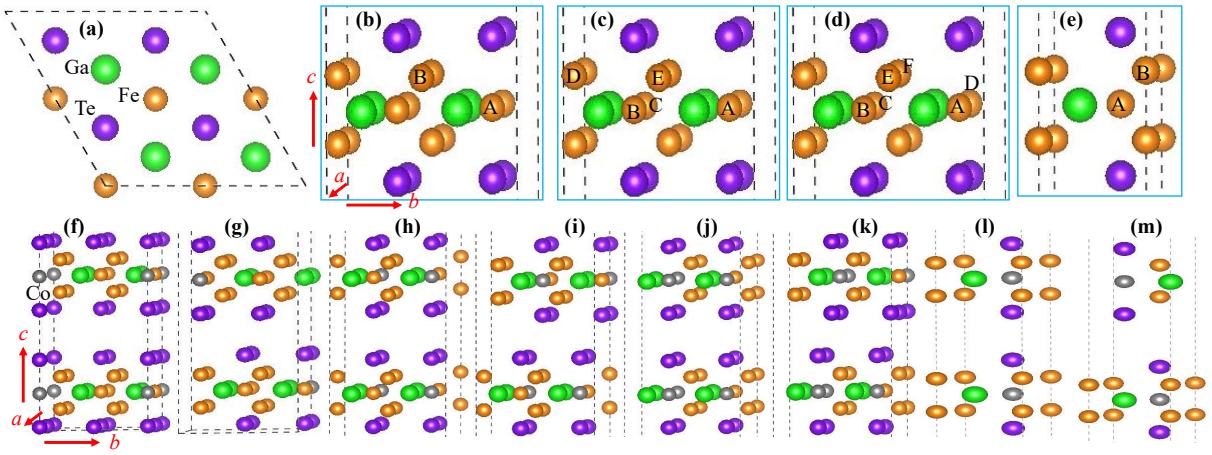

Fig. 1 Crystal structures **(a)** top view of the monolayer $Fe_{2.917}Co_{0.083}GaTe_2$, **(b)** side view of the monolayer $Fe_{2.917}Co_{0.083}GaTe_2$, **(c)** side view of the monolayer $Fe_{2.833}Co_{0.167}GaTe_2$, **(d)** side view of the monolayer $Fe_{2.75}Co_{0.25}GaTe_2$, **(e)** side view of the monolayer $Fe_{2.67}Co_{0.33}GaTe_2$, **(f)** AA stacking in the bilayer $Fe_{2.917}Co_{0.083}GaTe_2$, **(g)** AB stacking in the bilayer $Fe_{2.917}Co_{0.083}GaTe_2$, **(h)** AA stacking in the bilayer $Fe_{2.833}Co_{0.167}GaTe_2$, **(i)** AB stacking in the bilayer $Fe_{2.833}Co_{0.167}GaTe_2$, **(j)** AA stacking in the bilayer $Fe_{2.75}Co_{0.25}GaTe_2$, **(k)** AB stacking in the bilayer $Fe_{2.75}Co_{0.25}GaTe_2$, **(l)** AA stacking in the bilayer $Fe_{2.67}Co_{0.33}GaTe_2$, and **(m)** AB stacking in the bilayer $Fe_{2.67}Co_{0.33}GaTe_2$.

[36]. For calculating the AHC, we used the numerical tight-binding model Hamiltonian and employed the linear response Kubo formula approach [37]. A denser k-mesh of 150×150×1 is used to accurately construct real-space Wannier functions for calculating the AHC using a tight-binding Hamiltonian. The anomalous Nernst conductivity (ANC) is determined at 100 K using the Mott relation [38, 39].

3 Results and discussion

Herein, we investigate the magnetic properties of the $Fe_{3-x}Co_xGaTe_2$ (x = 0.083, 0.167, 0.250, and 0.330) systems for monolayer and bilayer thickness. Figures 1(a) and (b) show the top and side views of the optimized crystal structure of the pristine Fe_3GaTe_2 monolayer (2 × 2 × 1 supercell), respectively. The orange, green, and purple spheres represent the Fe, Ga, and Te atoms, respectively. For x = 0.083 doping concentration, we replace one Fe with Co in this (2 × 2 × 1) supercell. Since the Fe_3GaTe_2 monolayer has three sublayers, we consider two doping positions represented by A and B in Fig. 1(b); by replacing one Fe with one Co in the (i) central Fe layer and (ii) in the upper Fe layer (or bottom). According to our total energy calculations, the A-site doping is more stable than the B-site by an energy difference of 158 meV. For x = 0.167 doping concentration, we replace two Fe atoms with two Co atoms in the same supercell size as shown in Fig. 1(c). Here, we consider four different combinations. For instance, one Fe is replaced with a Co atom at A and the other Fe with Co atoms at B (C, D, and E). We find that the (AC) configuration is more stable than the (AB), (AD), and (AE) by an energy difference of 2 meV, 189 meV, and 180 meV. For x = 0.25 doping concentration, we replace three Fe atoms with three Co atoms as shown in Fig. 1(d). Here, we consider four possible combinations, (ABC), (ACD), (ACE), and (ACF), respectively. For instance, we replace the Fe at A, B, and C sites with Co in (ABC) configuration. The (ABC) combination becomes the most stable one with an energy difference of 11 meV, 197 meV, and 213 meV compared with the (ACD), (ACE), and (ACF) combinations. For x = 0.33 doping concentration, we consider a unit cell of the pristine Fe_3GaTe_2 and replace one Fe either from the central (A) or from the upper (B) layer as shown in Fig. 1(e). The central layer doping is more stable than the B site doping by an energy difference of 144 meV. Thus, we conclude that the Co always prefers the central layer in all doping concentrations in the monolayer $Fe_{3-x}Co_xGaTe_2$ (x = 0.083, 0.167, 0.250, and 0.330). The optimized lattice constants for all these stable crystal structures are provided in Table 1.

Using these monolayers $Fe_{3-x}Co_xGaTe_2$ (x = 0.083, 0.167, 0.250, and 0.330), we create a bilayer in every doping concentration. In bilayer $Fe_{3-x}Co_xGaTe_2$ (x = 0.083, 0.167, 0.250, and 0.330) systems, we consider two stacking orders; AA- and AB-type of stacking. As an illustration, we present the AA- and AB-type stacking with x = 0.083 in Figs. 1(f) and (g), respectively. In the AB-type stacking, the second layer is shifted by half of the lattice constant in the xy plane with respect to the first layer. For all Co doping concentrations, we find that the AB stacking is more stable than the AA type stacking. We present the details in Table S1 of the Electronic Supplementary Materials (ESM). The AB stacking order in the bilayer $Fe_{3-x}Co_xGaTe_2$ (x = 0.083, 0.167,

Table 1 Lattice constants of monolayer and bilayer $Fe_{3-x}Co_xGaTe_2$ (x = 0.083, 0.167, 0.250, and 0.330) along with interlayer distance (d) in the bilayer. The formation energy (E_F) of monolayer and exchange energy (ΔE_{ex}) of monolayer and bilayer.

System	$x = 0.083$	$x = 0.167$	$x = 0.25$	$x = 0.33$
$a = b$, Monolayer (in Å)	8.155	8.161	8.165	4.089
$a = b$, Bilayer (in Å)	8.058	8.064	8.072	4.040
d (in Å)	3.11	3.02	3.00	2.97
E_F molayer (meV/atom)	–166	–171	–175	–171
ΔE_{ex}(meV/cell) - Intralayer monolayer	983	884	760	581
ΔE_{ex}(meV/cell) - Interlayer bilayer	19	16	16	6

0.250, and 0.330) systems is the same as that reported in the experimentally fabricated Fe_3GaTe_2 system. In Table 1, we present the optimized lattice constants for bilayer $Fe_{3-x}Co_xGaTe_2$ (x = 0.083, 0.167, 0.250, and 0.330) systems along with the interlayer distances. The lattice constants of monolayer and bilayer $Fe_{3-x}Co_xGaTe_2$ are slightly increasing with the increasing doping concentration, while the interlayer distance in the bilayer decreases with increasing Co concentration. Note that we also consider random site dopings as shown in Figs. S1(a)–(j) of the Electronic Supplementary Materials (ESM) for bilayer $Fe_{3-x}Co_xGaTe_2$ with x = 0.083 and x = 0.33. However, all random site dopings are less stable compared with the regular site dopings with energy differences in the range of 163–368 meV/cell in x = 0.083 and 123–270 meV/cell in x = 0.33 doping concentrations. In the bilayer $Fe_{3-x}Co_xGaTe_2$ with x = 0.167 and x = 0.25, there are also several random site doping configurations. However, the energy differences in both the lowest (x = 0.083) and highest (x = 0.33) Co doping concentrations are very large. Therefore, we do not consider the random site doping in bilayer $Fe_{3-x}Co_xGaTe_2$ with x = 0.167 and x = 0.25.

Based on these optimized crystal structures, we calculate the formation energy using the following relation:

$$E_F = \frac{E_T - nE_{Fe} - 4E_{Ga} - 8E_{Te} - mE_{Co}}{N}. \quad (1)$$

Here, E_T, E_{Fe}, E_{Ga}, E_{Te}, E_{Co}, $n(m)$, and N represent the total energy of monolayer $Fe_{3-x}Co_xGaTe_2$, the chemical potential of the Fe atom, the chemical potential of the Ga atom, the chemical potential of the Te atom, the chemical potential of Co atom, number of Fe (Co) atoms, and the total number of atoms in the cell. The formation energy of monolayer $Fe_{3-x}Co_xGaTe_2$ (x = 0.083, 0.167, 0.250, and 0.330) is also provided in Table 1. The negative values of formation energies in all systems confirm their thermodynamical stability. Furthermore, we also calculate the phonon dispersion curves for monolayer $Fe_{3-x}Co_xGaTe_2$ (x = 0.083, 0.167, 0.250, and 0.330) to confirm the dynamical stabilities using the finite difference approach [40]. Here, we consider a 2 × 2 × 1 supercell, and the force criterion for the ionic step is set to 0.001 eV/Å. The phonon band structures for Co doping in monolayer $Fe_{3-x}Co_xGaTe_2$ (x = 0.083, 0.167, 0.250, and 0.330) are presented in Fig. S2 of the ESM. No trace of imaginary frequencies over the whole Brillouin zone is found in all the systems, indicating that monolayer $Fe_{3-x}Co_xGaTe_2$ (x = 0.083, 0.167, 0.250, and 0.330) systems are dynamically stable.

After confirming the stabilities, we now discuss the magnetic properties of the monolayer and bilayer $Fe_{3-x}Co_xGaTe_2$ (x = 0.083, 0.167, 0.250, and 0.330) systems. To find the magnetic ground state, we calculate the total energy difference between the antiferromagnetic (AFM) and ferromagnetic (FM) states ($\Delta E_{ex} = E_{AFM} - E_{FM}$). In the monolayer $Fe_{3-x}Co_xGaTe_2$ (x = 0.083, 0.167, 0.250, and 0.330) systems, the total energy difference is calculated by considering an intralayer exchange coupling, and the energy differences are 983, 884, 760, and 581 meV/cell. All the monolayer structures show the FM ground state. However, the exchange energy decreases with increasing Co concentrations. In the bilayer $Fe_{3-x}Co_xGaTe_2$ (x = 0.083, 0.167, 0.250, and 0.330) systems, we consider both intra and interlayer exchange interactions. The bilayer structures have also FM ground states. Here, we adopt the intra-layer exchange interaction from the monolayer, while the interlayer exchange energy (ΔE_{ex}) is provided in Table 1 for all bilayer systems. In the monolayer $Fe_{3-x}Co_xGaTe_2$ (x = 0.083, 0.167, 0.250, and 0.330) systems, the local magnetic moment of the Fe atom has position dependency. For instance, the central sublayer (Fe_{center}) has a local magnetic moment of 1.48 μ_B, 1.55 μ_B, and 1.62 μ_B in monolayer $Fe_{3-x}Co_xGaTe_2$ (x = 0.083, 0.167, and 0.25) systems, respectively. In $Fe_{3-x}Co_xGaTe_2$ (x = 0.333), all the Fe atoms in the central layer are replaced with Co atoms. Therefore, the magnetic moment of $Fe_{central}$ atom in this system is not listed here. In contrast, the top (or bottom) Fe atom ($Fe_{top(bottom)}$) has a higher local magnetic moment of 2.46 μ_B, 2.52 μ_B, 2.57 μ_B, and 2.60 μ_B at x = 0.083, 0.167, 0.250, and 0.330, respectively. On the other hand, the Co atom has a local magnetic moment of 0.81 μ_B, 0.83 μ_B, 0.85 μ_B, and 0.86 μ_B in the monolayer $Fe_{3-x}Co_xGaTe_2$ (x = 0.083, 0.167, 0.250, and 0.330) systems. Besides, a small negative magnetic moment of ~ –0.06 μ_B is induced in Te and ~ –0.08 μ_B in Ga atoms in monolayer $Fe_{3-x}Co_xGaTe_2$ (x = 0.083, 0.167, 0.250, and 0.330) systems. In the bilayer $Fe_{3-x}Co_xGaTe_2$ (x = 0.083, 0.167, 0.250, and 0.330) systems, the local magnetic moments of both Fe and Co atoms have a similar trend as found in the monolayer systems. The detailed descriptions are given in Table S2 of the ESM.

We also investigate the atom-to-atom exchange inter-

Table 2 Exchange parameter (J) in meV monolayer $Fe_{2.917}Co_{0.083}GaTe_2$.

Exchange interactions	J (1st NN) (meV)	J (2nd NN) (meV)	J (3rd NN) (meV)
Fe_{bottom}–Fe_{bottom} (Fe_{top}–Fe_{top})	2.91	0.46	0.41
$Fe_{central}$–$Fe_{central}$	–1.58	–0.42	1.44
Fe_{bottom}–Fe_{top}	81.79	–2.65	1.66
Fe_{bottom}–$Fe_{central}$ (Fe_{top}–$Fe_{central}$)	27.74	2.60	–1.33
$Fe_{central}$–$Co_{central}$	–1.69	–0.22	–0.12
$Co_{central}$–$Co_{central}$	0.19	–0.01	0
Fe_{bottom}–$Co_{central}$ (Fe_{top}–$Co_{central}$)	15.76	2.66	–1.20

Table 3 Exchange parameter (J) in meV for bilayer $Fe_{2.917}Co_{0.083}GaTe_2$.

Exchange interactions (intra-layer)	J (1st NN) (meV)	J (2nd NN) (meV)	J (3rd NN) (meV)
Fe_{bottom}–Fe_{bottom} (Fe_{top}–Fe_{top})	0.53	0.90	0.51
$Fe_{central}$–$Fe_{central}$	–0.96	–0.15	–0.07
Fe_{bottom}–Fe_{top}	77.38	–1.23	0.65
Fe_{bottom}–$Fe_{central}$ (Fe_{top}–$Fe_{central}$)	26.06	1.77	–0.68
$Fe_{central}$–$Co_{central}$	–1.34	0.04	0.0
$Co_{central}$–$Co_{central}$	0.07	0.01	–0.05
Fe_{bottom}–$Co_{central}$ (Fe_{top}–$Co_{central}$)	15.89	–0.84	–0.17
Exchange interactions (inter-layer)	J (1st NN) (meV)	J (2nd NN) (meV)	J (3rd NN) (meV)
Fe_{top} (layer 1)–Fe_{bottom} (layer 2)	0.09	0.24	–0.13
Fe_{top} (layer 1)–$Fe_{central}$ (layer 2)	0.54	0.27	–0.02
Fe_{top} (layer 1)–Fe_{top} (layer 2)	–0.07	–0.11	–0.04
Fe_{top} (layer 1)–$Co_{central}$ (layer 2)	0.15	–0.04	–0.03
$Fe_{central}$ (layer 1)–$Co_{central}$ (layer 2)	–0.22	0.02	0.01
$Co_{central}$ (layer 1)–$Co_{central}$ (layer 2)	–0.13	0.02	0.01
Fe_{bottom} (layer 1)–$Co_{central}$ (layer 2)	0.07	–0.01	–0.01

action as a function of an interatomic distance using Green's function method [41]. In this method, the Heisenberg Hamiltonian can be written as

$$H = -\sum_{ij} J_{ij}(m_i \cdot m_j), \tag{2}$$

where $m_i(m_j)$ and J_{ij} are the normalized magnetic moments at site $i(j)$ and the Heisenberg isotropic exchange. In all the studied systems, we consider the pairs (i, j) with up to the third nearest neighbor (NN). We select seven different intralayer spin pairs; Fe_{bottom}–Fe_{bottom} (equivalently Fe_{top}–Fe_{top}), $Fe_{central}$–$Fe_{central}$, Fe_{bottom}–Fe_{top}, Fe_{bottom}–$Fe_{central}$ (equivalently Fe_{top}–$Fe_{central}$), $Fe_{central}$–$Co_{central}$, $Co_{central}$–$Co_{central}$, and Fe_{bottom}–$Co_{central}$ (equivalently Fe_{top}–$Co_{central}$) in the monolayer $Fe_{3-x}Co_xGaTe_2$ (x = 0.083, 0.167, 0.250, and 0.330) systems. In the bilayer structure, we consider both intralayer and inter-layer exchange interactions. As an illustration, we present the J_{ij} up to the third NN of the monolayer and bilayer $Fe_{2.917}Co_{0.083}GaTe_2$ system in Tables 2 and 3. The positive (negative) exchange J values favor a ferromagnetic (antiferromagnetic) interaction. In the monolayer $Fe_{2.917}Co_{0.083}GaTe_2$ system, the dominant exchange coupling originates from the first NN Fe_{bottom}–Fe_{top} interaction followed by the first NN Fe_{bottom}–$Fe_{central}$ and Fe_{bottom}–$Co_{central}$ interaction as shown in Table 2.

In the bilayer $Fe_{2.917}Co_{0.083}GaTe_2$ system, the intralayer interactions show the same trend as in the monolayer $Fe_{2.917}Co_{0.083}GaTe_2$ system, although the magnitudes are slightly changed. For instance, the main contribution is dominated by the first NN Fe_{bottom}–Fe_{top} exchange interactions with $J \sim 77.38$ meV as shown in Table 3. The inter-layer exchange interaction is quite weak compared with the intra-layer interaction. For instance, it is only 0.54 meV for the first NN Fe_{top} (layer 1)–$Fe_{central}$ (layer 2). Note that the effective J values for monolayer (18.34 meV) and bilayer (18.03 meV) $Fe_{2.917}Co_{0.083}GaTe_2$ systems using the Green's function are in close agreement with (20.19 meV) and (17.77 meV) obtained from VASP. A similar feature is found in other systems as well.

Next, we calculated the spin-projected electronic band structures including the spin–orbit coupling (SOC) for the monolayer and bilayer $Fe_{3-x}Co_xGaTe_2$ (x = 0.083, 0.167, 0.250, and 0.330) systems. Figures 2(a) and (b) show spin-projected band structures including SOC for monolayer and bilayer $Fe_{2.917}Co_{0.083}GaTe_2$ systems. The band structures for all the other systems are given in Figs. S3(a)–(f) of the ESM. The horizontal zero line represents the Fermi level. We find conventional metallic band structures in monolayer and bilayer $Fe_{3-x}Co_xGaTe_2$ (x = 0.083, 0.167, 0.250, and 0.330) systems. For comparison, we also plot the spin projected band structure including SOC for pristine monolayer and bilayer Fe_3GaTe_2 systems in Figs. S4(a) and (b) of the ESM. We also calculate the magnetocrystalline anisotropy energy (MAE) due to SOC. All the systems show perpendicular magnetic anisotropy. The calculated results are presented in Table 4. Note that the MAE of the pristine Fe_3GaTe_2 monolayer is 0.20 meV/atom (per Fe atom), while it is increased to 0.32 meV/atom in bilayer Fe_3GaTe_2 [26]. From Table 4, it is clear that the MAE is largely enhanced with increasing Co concentration in both monolayer and bilayer $Fe_{3-x}Co_xGaTe_2$ (x = 0.083, 0.167, 0.250, and 0.330) systems.

To understand this out-of-plane anisotropy, we analyze the SOC matrix elements of the monolayer $Fe_{2.917}Co_{0.083}GaTe_2$. Figures 3(a)–(d) show the SOC

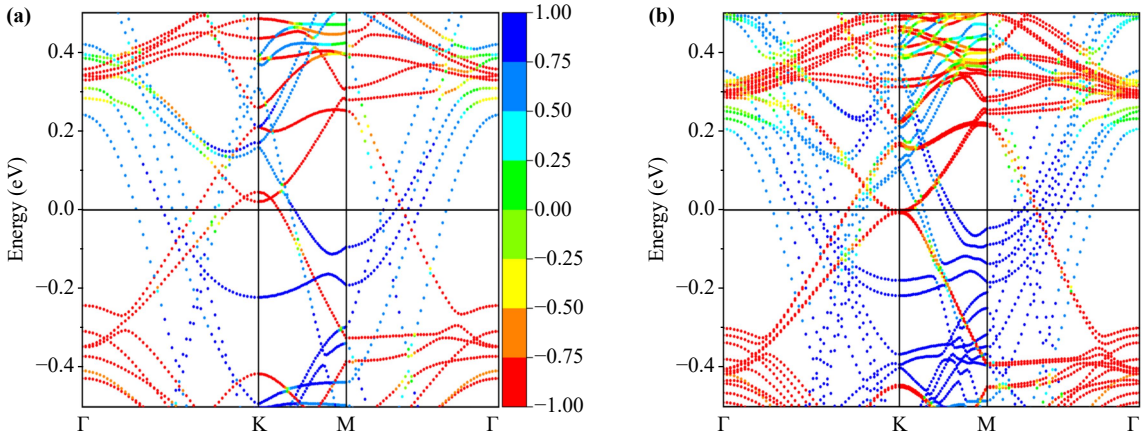

Fig. 2 Spin-projected band structures including spin–orbit coupling **(a)** monolayer $Fe_{2.917}Co_{0.083}GaTe_2$, **(b)** bilayer $Fe_{2.917}Co_{0.083}GaTe_2$.

Table 4 Magnetocrystalline anisotropy (in meV/atom) and Curie temperatures of monolayer and bilayer.

System	$x = 0.083$	$x = 0.167$	$x = 0.25$	$x = 0.33$
Monolayer MAE	0.49	0.75	1.07	1.48
Bilayer MAE	0.53	0.76	1.04	1.37
Monolayer T_C (K)	253	230	200	163
Bilayer T_C (K)	269	240	210	173

matrix elements of the Te, Fe-top, Fe-center, and Co atoms in monolayer $Fe_{2.917}Co_{0.083}GaTe_2$ respectively. Although the magnetic moment mainly originates from Fe and Co atoms, a small negative magnetic moment is found in the Te atom. Nonetheless, the dominant contribution to the MAE originates from the Te atoms. The SOC through the $(p_x–p_y)$ orbitals of the Te atom results in the out-of-plane anisotropy as shown in Fig. 3(a), while the contributions to the MAE from the Fe-top and Fe-center (Co) atoms are rather weak as shown in Figs. 3(b)–(d). For comparison, the SOC matrix elements of Te, Fe-top, and Fe-center atoms in pristine Fe_3GaTe_2 monolayer is presented in Fig. S5 of the ESM. In Fig. S6 of the ESM, we also present the contribution to the total MAE of every system from Fe, Te, and Co atoms in different layers in monolayer and bilayer $Fe_{3-x}Co_xGaTe_2$ (x = 0.083, 0.167, 0.25, and 0.33) systems. We now calculate the Curie temperatures using the Metropolis Monte Carlo simulation. Here, we use the Heisenberg model Hamiltonian with single-ion magnetic anisotropy,

$$\widehat{H} = -\sum_{i,j} J\widehat{m}_i \cdot \widehat{m}_j - k_2 \sum_i m_z^2. \quad (3)$$

Here, J represents the exchange parameter, while $\widehat{m}_{i(j)}$, k_2, and m_z are the magnetic moments (in μ_B) at sites $i(j)$, single-ion anisotropy constant, and spin pointing along the easy axis, respectively. The exchange parameter J is calculated using the relation $J = \frac{E_{ex}}{nm^2}$. Here E_{ex} is the

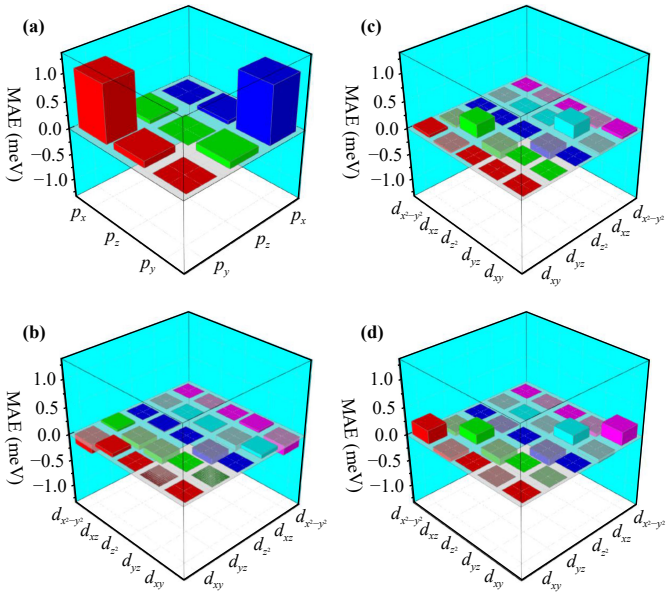

Fig. 3 Orbital resolved MAE of monolayer $Fe_{2.917}Co_{0.083}GaTe_2$ **(a)** Te atom, **(b)** Fe-top atom, **(c)** Fe-center atom, **(d)** Co atom.

exchange energy difference between FM and AFM, n represents the number of magnetic atoms and m denotes the magnetic moment. A supercell of (50 × 50 × 1) with periodic boundary conditions in xy-plane is used to calculate the temperature-dependent magnetization curve. All the systems are equilibrated for time steps of 10 000 followed by a statistical average over another 10 000 steps to evaluate the average magnetization [34]. Figures 4(a)–(h) show the temperature-dependent magnetization curves of monolayer and bilayer $Fe_{3-x}Co_x$-$GaTe_2$ (x = 0.083, 0.167, 0.250, and 0.330) systems. For comparison, we present the temperature-dependent magnetization curves for pristine monolayer and bilayer Fe_3GaTe_2 systems in Figs. S7(a) and (b) of the ESM.

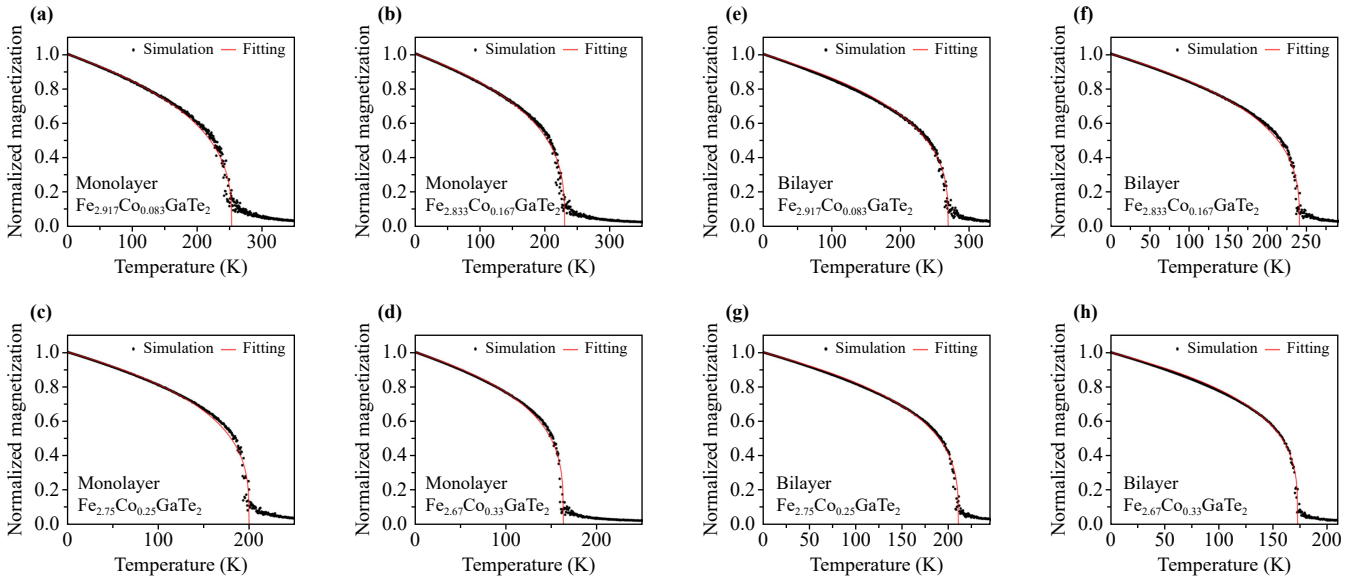

Fig. 4 Temperature-dependent magnetization curves for **(a)** monolayer $Fe_{2.917}Co_{0.083}GaTe_2$, **(b)** monolayer $Fe_{2.833}Co_{0.167}GaTe_2$, **(c)** monolayer $Fe_{2.75}Co_{0.25}GaTe_2$, **(d)** monolayer $Fe_{2.67}Co_{0.33}GaTe_2$, **(e)** bilayer $Fe_{2.917}Co_{0.083}GaTe_2$, **(f)** bilayer $Fe_{2.833}Co_{0.167}GaTe_2$, **(g)** bilayer $Fe_{2.75}Co_{0.25}GaTe_2$, **(h)** bilayer $Fe_{2.67}Co_{0.33}GaTe_2$.

The temperature-dependent magnetization curves are fitted with the Curie–Bloch equation $m(T) = (1 - T/T_C)^{\beta}$. Here, T_C and β are the Curie temperature and critical exponent, respectively. The value of the β is ranging from 0.28 to 0.34 in all the systems. Note that the Curie temperature (T_C) is primarily affected by the exchange energy; higher exchange energy correlates with a higher T_C for the system, whereas the influence of the MAE on the Curie temperature is rather weak. The Curie temperature of monolayer and bilayer $Fe_{3-x}Co_xGaTe_2$ ($x =$ 0.083, 0.167, 0.250, and 0.330) systems are given in Table 2. The Curie temperatures of monolayer and bilayer $Fe_{2.917}Co_{0.083}GaTe_2$ are 253 K and 269 K, respectively. The Curie temperature is decreasing in both monolayer and bilayer systems with increasing the Co doping ratio. The decrease in Curie temperatures is due to the decrease in exchange energy in the presence of Co.

We also calculate the transverse transport properties; anomalous Hall conductivity (AHC), anomalous Nernst conductivity (ANC), and anomalous thermal Hall conductivity (ATHC). By integrating the Berry curvature throughout the whole Brillouin zone (BZ), the AHC (σ_{xy}) can be found using the Berry phase theory and the linear response Kubo formula as given below:

$$\sigma_{xy} = -\frac{e^2}{\hbar}\sum\nolimits_n \int_{BZ}^{BZ} \frac{\mathrm{d}k}{(2\pi)^3} f_n(k)\,\Omega_{n,z}(k)\,, \tag{4}$$

where e, f_n, and $\Omega_{n,z}(k)$ are the elementary charge, Fermi–Dirac distribution function, and Berry curvature. The Berry curvature can be calculated by the following relations:

$$\Omega_{n,z}(k) = -\sum_n f_n \Omega_n(k)\,, \tag{5}$$

$$\Omega_n(k) = -2Im\sum_{m\neq n} \frac{\langle u_{nk}|\nu_x|u_{mk}\rangle\langle u_{mk}|\nu_y|u_{nk}\rangle}{(E_{mk} - E_{nk})^2}. \tag{6}$$

Here, $\nu_{x,y}$, $u_{nk}(u_{mk})$, and $E_{nk}(E_{mk})$ are the velocity operators, the periodic part of the Bloch wave function with eigenvalue $E_{nk}(E_{mk})$. The Berry curvature is calculated using the Wannier interpolation technique [36], in which a set of maximally localized Wannier functions (MLWFs) are constructed from the Bloch wave functions. A Fourier-transformed Wannier Hamiltonian is calculated using the projected Bloch wave functions onto these MLWFs. Figures 5(a) and (b) show the Co concentration dependent AHC of the monolayer and bilayer $Fe_{3-x}Co_x$-$GaTe_2$ ($x =$ 0.083, 0.167, 0.250, and 0.330) systems. For comparison, we also present the AHC of the pristine structure. Compared with the AHC of the pristine monolayer structure, the magnitude of AHC is increased with Co doping at zero chemical potential (no carrier doping) although no monotonic behavior is observed as shown in Fig. 5(a) inset. Particularly, the largest AHC of –294 S/cm is obtained in monolayer $Fe_{2.75}Co_{0.25}GaTe_2$. In the bilayer structure, the AHC is also increased compared with that of the pristine bilayer system. Unlike in the monolayer case, the AHC of the Co doped structures has no substantial change with increasing the Co concentration at zero chemical potential as shown in Fig. 5(b) inset. The most noticeable behavior is found in the hole-doped bilayer system. Particularly, the bilayer $Fe_{2.917}Co_{0.083}GaTe_2$ shows an AHC of –578 S/cm at a

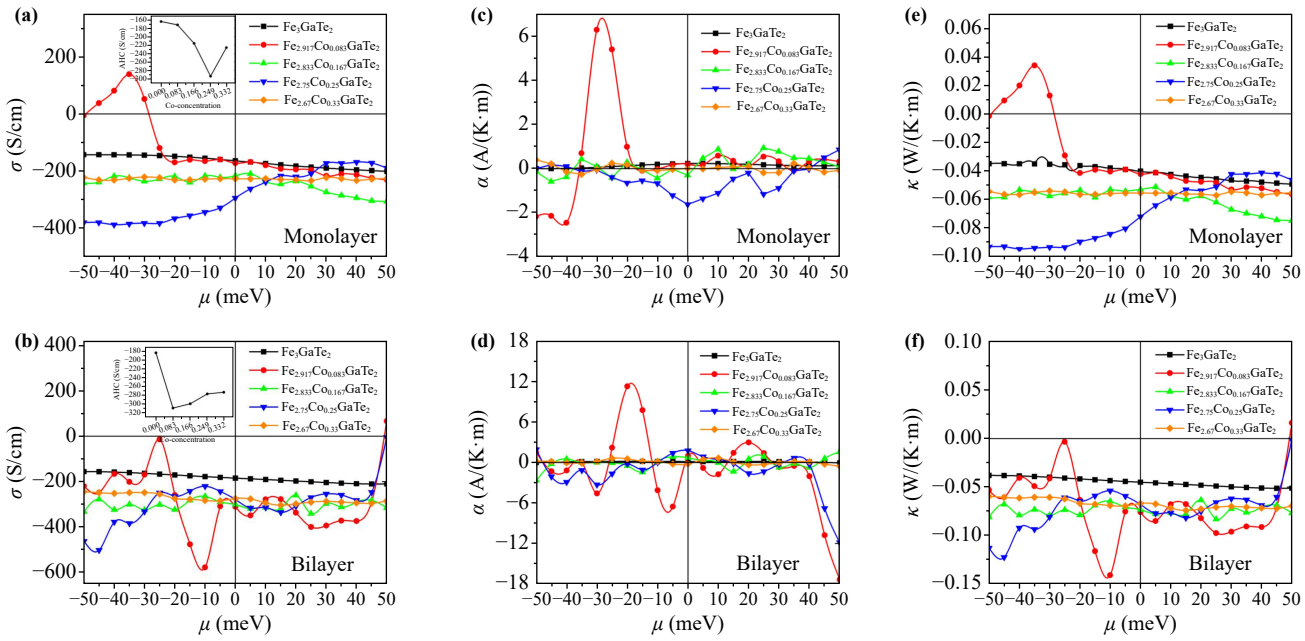

Fig. 5 Thickness-dependent **(a, b)** anomalous Hall conductivity as a function of chemical potential for monolayer and bilayer $Fe_{3-x}Co_xGaTe_2$ systems, **(c, d)** anomalous Nernest conductivity as a function of chemical potential for monolayer and bilayer $Fe_{3-x}Co_xGaTe_2$ systems, and **(e, f)** anomalous thermal Hall conductivity as a function of chemical potential for monolayer and bilayer $Fe_{3-x}Co_xGaTe_2$ systems.

small chemical potential shifting of just –10 meV. This value is substantially larger than those found in Fe_3GeTe_2 (360 S/cm) and $Co_3Sn_2S_2$ (150 S/cm) [42, 43]. Besides, it is also almost three times larger than the pristine bilayer Fe_3GaTe_2 at the same chemical potential. We also calculate the longitudinal electrical conductivity using the Boltzmann approach as implemented in the BoltzTrap2 code [44]. Since our systems are metallic, we apply the typical relaxation time of metallic systems (~10^{-14} s) to calculate the longitudinal electrical conductivity σ_{xx} of monolayer and bilayer $Fe_{3-x}Co_xGaTe_2$ systems. The electrical conductivity σ_{xx} as a function of chemical potential for all the systems is presented in Figs. S8(a)–(h) of the ESM. We find that the σ_{xx} from 1.4×10^5 to 10.7×10^5 S/cm. Note that it has been identified that the $\sigma_{xy}^{\mathrm{AH}}$ is determined by scattering-independent or purely intrinsic Berry curvature if the σ_{xx} is ranged from 10^4 to 10^6 S/cm [45]. Since the longitudinal conductivities for all our studied systems are within this critical range, we infer that the dominant contribution to $\sigma_{xy}^{\mathrm{AH}}$ stems from the intrinsic Berry curvature.

Figures 5(c) and (d) show the ANC at 100 K for monolayer and bilayer $Fe_{3-x}Co_xGaTe_2$ (x = 0.083, 0.167, 0.250, and 0.330) systems using the Mott relation [38, 39]:

$$\alpha_{xy} = -\frac{\pi^2 k_{\mathrm{B}}^2 T}{3e} \frac{\mathrm{d}\sigma_{xy}}{\mathrm{d}\varepsilon}\bigg|_{\varepsilon=\mu}. \tag{7}$$

Note that the ANC is related to the first derivative of the AHC. Figure 5(c) shows the ANC in monolayer systems. The largest ANC of –1.63 A/(K·m) is obtained in the $Fe_{2.75}Co_{0.25}GaTe_2$ system at zero chemical potential. Moreover, the ANC of the $Fe_{2.917}Co_{0.083}GaTe_2$ system is largely enhanced to 6.03 A/(K·m) at a small chemical potential of –30 meV. Figure 5(d) shows the ANC of the bilayer systems. Like in the monolayer case, the highest ANC of 1.79 A/(K·m) is found in the bilayer $Fe_{2.75}Co_{0.25}GaTe_2$ system at zero chemical potential. However, the ANC of the bilayer $Fe_{2.917}Co_{0.083}GaTe_2$ system is greatly enhanced to –6.52 A/(K·m) at –5 meV and 11.30 A/(K·m) at a chemical potential of –20 meV. This is almost twenty times larger than that found in the four-layer pristine Fe_3GaTe_2 [0.55 A/(K·m)] at –45 meV [26]. Besides, the obtained ANC at 100 K is also very large compared to the experimentally reported 2D Fe_3GeTe_2 thin film [0.3 A/(K·m) at 140 K] and also theoretically reported half metallic $FeCl_3$ monolayer [–0.45 A/(K·m) at 100 K] [24, 43].

We also calculate the ATHC which is a measure of the transverse thermal current generated in a material due to a longitudinal temperature gradient. The ATHC can be calculated using the following linear response relation [46]:

$$\kappa_{xy} = \frac{1}{\hbar T} \int \mathrm{d}\varepsilon \left[-(\varepsilon - \mu)^2 \frac{\partial f}{\partial \varepsilon} \right] \sigma_{xy}. \tag{8}$$

The Wiedemann–Franz (WF) law correlates both AHC and ATHC in the following relation:

$$\kappa_{xy} = L_{xy} \sigma_{xy} T, \tag{9}$$

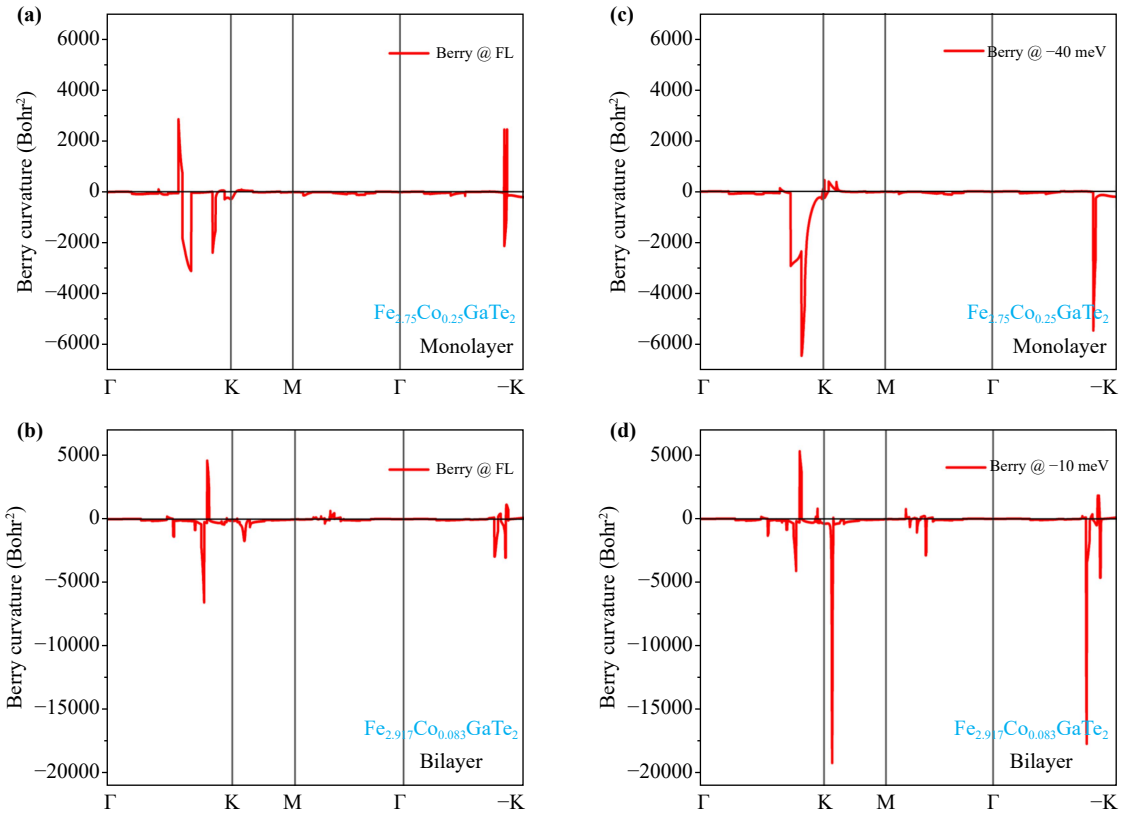

Fig. 6 Berry curvature along high symmetry lines for **(a)** monolayer $Fe_{2.75}Co_{0.25}GaTe_2$ at zero chemical potential, **(b)** bilayer $Fe_{2.917}Co_{0.083}GaTe_2$ at zero chemical potential, **(c)** monolayer $Fe_{2.75}Co_{0.25}GaTe_2$ at –40 meV and **(d)** bilayer $Fe_{2.917}Co_{0.083}GaTe_2$ at –10 meV.

where L_{xy} having a value of ~2.44 × 10^{-8} Ω·W/K^2 is known as the Lorenz number. Figure 5(e) shows the ATHC of the monolayer systems at 100 K. Since the AHC and ATHC are correlated to each other, both AHC and ATHC display the same spectral shapes. At zero chemical potential, the ATHC is rather small ~ –0.07 W/(K·m) as maximum in the monolayer $Fe_{2.75}Co_{0.25}GaTe_2$ and bilayer $Fe_{2.917}Co_{0.083}GaTe_2$ systems as shown in Figs. 5(e) and (f). However, the ATHC of the bilayer $Fe_{2.917}Co_{0.083}GaTe_2$ is greatly enhanced to –0.14 W/(K·m) at a chemical potential of –10 meV. This is larger than that found in four-layer pristine Fe_3GaTe_2 [–0.105 W/(K·m)] [26] and close to the reported giant ATHC in Weyl semimetal $Co_3Sn_2S_2$ [~0.14 W/(K·m)] at 80 K [17]. The AHC is a key factor for governing all the transverse transport coefficients (AHC, ANC, and ATHC). Therefore, we analyze the AHC. As a representative illustration, we select monolayer $Fe_{2.75}Co_{0.25}GaTe_2$ and bilayer $Fe_{2.917}Co_{0.083}GaTe_2$ systems. Figures 6(a) and (b) show the Berry curvatures along the high symmetry directions for the monolayer $Fe_{2.75}Co_{0.25}GaTe_2$ and bilayer $Fe_{2.917}Co_{0.083}GaTe_2$ systems at zero chemical potential [i.e., at the Fermi level (FL)]. The Berry curvatures for all other systems at FL are provided in Fig. S9 of the ESM. The positive and negative Berry curvature leads to positive and negative AHC. The negative and positive Berry curvature can also originate from the general k-points in the BZ, but here for a qualitative analysis, we only consider along the high symmetry lines. In the monolayer $Fe_{2.75}Co_{0.25}GaTe_2$ at the FL, two negative peaks and positive peaks are found in the Γ–K path as shown in Fig. 6(a). The negative and positive Berry curvatures compensate resulting in a suppression of the AHC. Similarly, in the bilayer $Fe_{2.917}Co_{0.083}GaTe_2$ system at FL, a large negative peak is found from Γ to K point along with a comparatively small positive Berry curvature peak as shown in Fig. 6(b). Thus, the AHCs of both mono (–294 S/cm) and bilayer (–311 S/cm) structures are almost the same. However, the negative peaks are substantially enhanced at a chemical potential of –40 meV in the monolayer $Fe_{2.75}Co_{0.25}GaTe_2$ and –10 meV in the bilayer $Fe_{2.917}Co_{0.083}GaTe_2$ system. Particularly, the enhancement of the Berry curvature in the bilayer is more noticeable. Thus, we find that the bilayer structure shows the most outstanding transverse transport properties.

4 Conclusion

In summary, we investigate the magnetic ground state,

magnetocrystalline anisotropy, Curie temperature, and transverse transport properties of monolayer and bilayer $Fe_{3-x}Co_xGaTe_2$ (x = 0.083, 0.167, 0.250, and 0.330) systems. Both mono and bilayer structures have FM ground states with ordinary metallic behavior. All the systems show out-of-plane magnetic anisotropy with large magnitudes in both monolayer and bilayer $Fe_{3-x}Co_xGaTe_2$ (x = 0.083, 0.167, 0.250, and 0.330). For instance, both monolayer and bilayer $Fe_{2.917}Co_{0.083}GaTe_2$ have MAEs of 0.49 and 0.53 meV/atom, respectively, and these are greatly enhanced with increasing Co concentration. We obtain the MAEs of 1.48 meV/atom and 1.37 meV/atom in the monolayer and bilayer $Fe_{2.67}Co_{0.33}GaTe_2$, respectively. These MAEs are more than twice larger than those found in the pristine monolayer and bilayer Fe_3GaTe_2. The monolayer and bilayer $Fe_{2.917}Co_{0.083}GaTe_2$ systems have Curie temperatures of 253 K and 269 K, but the Curie temperatures are decreased with increasing Co concentration. For instance, these Curie temperatures are decreased to 163 K and 173 K in monolayer and bilayer $Fe_{2.67}Co_{0.33}GaTe_2$ systems. We find an AHC of –294 S/cm in the monolayer $Fe_{2.75}Co_{0.25}GaTe_2$ at zero chemical potential, but this is further enhanced to –387 S/cm at a small chemical potential of –40 meV. Similarly, an AHC of –311 S/cm is found in the bilayer $Fe_{2.917}Co_{0.083}GaTe_2$ system at zero chemical potential, and this is increased to –578 S/cm at –10 meV chemical potential. Besides, the ANC is largely enhanced to 6.03 A/(K·m) at –30 meV and 11.30 A/(K·m) at –20 meV in monolayer and bilayer $Fe_{2.917}Co_{0.083}GaTe_2$ systems respectively at 100 K. Furthermore, the ATHC in the bilayer $Fe_{2.917}Co_{0.083}GaTe_2$ structure at 100 K reaches –0.14 W/(K·m) at a chemical potential of –10 meV which is comparable to the giant ATHC of Weyl semimetal $Co_3Sn_2S_2$ [~0.14 W/(K·m)] at 80 K. Overall, we propose that the $Fe_{3-x}Co_xGaTe_2$ structure shows better anomalous transverse transport performance than the pristine Fe_3GaTe_2. These findings may stimulate further experimental verifications.

Declarations The authors declare that they have no competing interests and there are no conflicts.

Author contributions J. H. conceived the idea of this study; I. K. performed DFT calculations; J. H. and I. K. wrote and revised the manuscript.

Electronic supplementary materials The online version contains supplementary material available at https://doi.org/10.1007/s11467-024-1424-5 and https://journal.hep.com.cn/fop/EN/10.1007/s11467-024-1424-5. Supporting information includes the information about different random site Co doping in bilayer $Fe_{3-x}Co_xGaTe_2$, phonon dispersion curves for monolayer $Fe_{3-x}Co_xGaTe_2$, average local magnetic moments in bilayer $Fe_{3-x}Co_xGaTe_2$, spin projected band structures including SOC for monolayer and bilayer systems, MAE contributions, temperature dependent magnetization curves, thickness-dependent longitudinal conductivity, and Barry curvature along high symmetry lines for monolayer and bilayer $Fe_{3-x}Co_xGaTe_2$ systems.

Acknowledgements This work was supported by the National Research Foundation of Korea (NRF) grant funded by the Korean government (MSIT) (No. 2022R1A2C1004440) and the Supercomputing Center/Korea Institute of Science and Technology Information with supercomputing resources including technical support (KSC-2023-CRE-0190).

References and notes

1. O. V. Yazyev, Emergence of magnetism in graphene materials and nanostructures, *Rep. Prog. Phys.* 73(5), 056501 (2010)
2. O. V. Yazyev and L. Helm, Defect-induced magnetism in graphene, *Phys. Rev. B* 75(12), 125408 (2007)
3. I. Khan and J. Hong, Magnetic properties of transition metal Mn, Fe and Co dimers on monolayer phosphorene, *Nanotechnology* 27(38), 385701 (2016)
4. Y. W. Son, M. L. Cohen, and S. G. Louie, Half-metallic graphene nanoribbons, *Nature* 444(7117), 347 (2006)
5. B. Huang, G. Clark, E. Navarro-Moratalla, D. R. Klein, R. Cheng, K. L. Seyler, D. Zhong, E. Schmidgall, M. A. McGuire, D. H. Cobden, W. Yao, D. Xiao, P. Jarillo-Herrero, and X. Xu, Layer-dependent ferromagnetism in a van der Waals crystal down to the monolayer limit, *Nature* 546(7657), 270 (2017)
6. C. Gong, L. Li, Z. Li, H. Ji, A. Stern, Y. Xia, T. Cao, W. Bao, C. Wang, Y. Wang, Z. Q. Qiu, R. J. Cava, S. G. Louie, J. Xia, and X. Zhang, Discovery of intrinsic ferromagnetism in two-dimensional van der Waals crystals, *Nature* 546(7657), 265 (2017)
7. D. J. O'Hara, T. Zhu, A. H. Trout, A. S. Ahmed, Y. K. Luo, C. H. Lee, M. R. Brenner, S. Rajan, J. A. Gupta, D. W. McComb, and R. K. Kawakami, Room temperature intrinsic ferromagnetism in epitaxial manganese selenide films in the monolayer limit, *Nano Lett.* 18(5), 3125 (2018)
8. M. Bonilla, S. Kolekar, Y. Ma, H. C. Diaz, V. Kalappattil, R. Das, T. Eggers, H. R. Gutierrez, M. H. Phan, and M. Batzill, Strong room-temperature ferromagnetism in VSe_2 monolayers on van der Waals substrates, *Nat. Nanotechnol.* 13(4), 289 (2018)
9. B. Huang, G. Clark, E. Navarro-Moratalla, D. R. Klein, R. Cheng, K. L. Seyler, D. Zhong, E. Schmidgall, M. A. McGuire, D. H. Cobden, W. Yao, D. Xiao, P. Jarillo-Herrero, and X. Xu, Layer-dependent ferromagnetism in a van der Waals crystal down to the monolayer limit, *Nature* 546(7657), 270 (2017)
10. C. Gong, L. Li, Z. Li, H. Ji, A. Stern, Y. Xia, T. Cao, W. Bao, C. Wang, Y. Wang, Z. Q. Qiu, R. J. Cava, S. G. Louie, J. Xia, and X. Zhang, Discovery of intrinsic ferromagnetism in two-dimensional van der Waals crystals, *Nature* 546(7657), 265 (2017)
11. F. Xue, Y. Hou, Z. Wang, and R. Wu, Two-dimensional ferromagnetic van der Waals $CrCl_3$ monolayer with enhanced anisotropy and Curie temperature, *Phys. Rev.*

B 100(22), 224429 (2019)

12. B. Li, Z. Wan, C. Wang, P. Chen, B. Huang, X. Cheng, Q. Qian, J. Li, Z. Zhang, G. Sun, B. Zhao, H. Ma, R. Wu, Z. Wei, Y. Liu, L. Liao, Y. Ye, Y. Huang, X. Xu, X. Duan, W. Ji, and X. Duan, Van der Waals epitaxial growth of air-stable $CrSe_2$ nanosheets with thickness-tunable magnetic order, *Nat. Mater.* 20(6), 818 (2021)
13. Y. Wu, Y. Hu, C. Wang, X. Zhou, X. Hou, W. Xia, Y. Zhang, J. Wang, Y. Ding, J. He, P. Dong, S. Bao, J. Wen, Y. Guo, K. Watanabe, T. Taniguchi, W. Ji, Z. J. Wang, and J. Li, Fe-intercalation dominated ferromagnetism of van der Waals Fe_3GeTe_2, *Adv. Mater.* 35(36), 2302568 (2023)
14. Z. Fei, B. Huang, P. Malinowski, W. Wang, T. Song, J. Sanchez, W. Yao, D. Xiao, X. Zhu, A. F. May, W. Wu, D. H. Cobden, J. H. Chu, and X. Xu, Two-dimensional itinerant ferromagnetism in atomically thin Fe_3GeTe_2, *Nat. Mater.* 17(9), 778 (2018)
15. Y. Deng, Y. Yu, Y. Song, J. Zhang, N. Z. Wang, Z. Sun, Y. Yi, Y. Z. Wu, S. Wu, J. Zhu, J. Wang, X. H. Chen, and Y. Zhang, Gate-tunable room-temperature ferromagnetism in two-dimensional Fe_3GeTe_2, *Nature* 563(7729), 94 (2018)
16. G. Zhang, F. Guo, H. Wu, X. Wen, L. Yang, W. Jin, W. Zhang, and H. Chang, Above-room-temperature strong intrinsic ferromagnetism in 2D van der Waals Fe_3GaTe_2 with large perpendicular magnetic anisotropy, *Nat. Commun.* 13(1), 5067 (2022)
17. A. Roy Karmakar, S. Nandy, A. Taraphder, and G. P. Das, Giant anomalous thermal Hall effect in tilted type-I magnetic Weyl semimetal $Co_3Sn_2S_2$, *Phys. Rev. B* 106(24), 245133 (2022)
18. C. Wuttke, F. Caglieris, S. Sykora, F. Scaravaggi, A. U. B. Wolter, K. Manna, V. Süss, C. Shekhar, C. Felser, B. Büchner, and C. Hess, Berry curvature unravelled by the anomalous Nernst effect in Mn_3Ge, *Phys. Rev. B* 100(8), 085111 (2019)
19. T. Jungwirth, Q. Niu, and A. H. MacDonald, Anomalous Hall effect in ferromagnetic semiconductors, *Phys. Rev. Lett.* 88(20), 207208 (2002)
20. M. Onoda and N. Nagaosa, Quantized anomalous Hall effect in two-dimensional ferromagnets: Quantum Hall effect in metals, *Phys. Rev. Lett.* 90(20), 206601 (2003)
21. Y. Yao, L. Kleinman, A. H. MacDonald, J. Sinova, T. Jungwirth, D. Wang, E. Wang, and Q. Niu, First principles calculation of anomalous Hall conductivity in ferromagnetic bcc Fe, *Phys. Rev. Lett.* 92(3), 037204 (2004)
22. X. Lin and J. Ni, Layer-dependent intrinsic anomalous Hall effect in Fe_3GeTe_2, *Phys. Rev. B* 100(8), 085403 (2019)
23. X. J. Dong, J. Y. You, B. Gu, and G. Su, Strain-induced room-temperature ferromagnetic semiconductors with large anomalous Hall conductivity in two-dimensional $Cr_2Ge_2Se_6$, *Phys. Rev. Appl.* 12(1), 014020 (2019)
24. R. Syariati, S. Minami, H. Sawahata, and F. Ishii, First-principles study of anomalous Nernst effect in half-metallic iron dichloride monolayer, *APL Mater.* 8(4), 041105 (2020)
25. A. T. Breidenbach, H. Yu, T. A. Peterson, A. P. McFadden, W. K. Peria, C. J. Palmstrøm, and P. A. Crowell, Anomalous Nernst and Seebeck coefficients in epitaxial thin film $Co_2MnAl_xSi_{1-x}$ and Co_2FeAl, *Phys. Rev. B* 105(14), 144405 (2022)
26. B. Marfoua and J. Hong, Large anomalous transverse transport properties in atomically thin 2D Fe_3GaTe_2, *NPG Asia Mater.* 16, 6 (2024)
27. H. Chen, S. Asif, K. Dolui, Y. Wang, J. Támara-Isaza, V. M. L. D. P. Goli, M. Whalen, X. Wang, Z. Chen, H. Zhang, K. Liu, D. Jariwala, M. B. Jungfleisch, C. Chakraborty, A. F. May, M. A. McGuire, B. K. Nikolic, J. Q. Xiao, and M. J. H. Ku, Above-room-temperature ferromagnetism in thin van der Waals flakes of cobalt-substituted Fe_5GeTe_2, *ACS Appl. Mater. Interfaces* 15(2), 3287 (2023)
28. G. Kresse and J. Furthmüller, Efficiency of *ab-initio* total energy calculations for metals and semiconductors using a plane-wave basis set, *Comput. Mater. Sci.* 6(1), 15 (1996)
29. G. Kresse and J. Furthmüller, Efficient iterative schemes for ab initio total-energy calculations using a plane-wave basis set, *Phys. Rev. B* 54(16), 11169 (1996)
30. D. Hobbs, G. Kresse, and J. Hafner, Fully unconstrained noncollinear magnetism within the projector augmented-wave method, *Phys. Rev. B* 62(17), 11556 (2000)
31. S. Grimme, J. Antony, S. Ehrlich, and H. Krieg, A consistent and accurate *ab initio* parametrization of density functional dispersion correction (DFT-D) for the 94 elements H–Pu, *J. Chem. Phys.* 132(15), 154104 (2010)
32. S. Grimme, S. Ehrlich, and L. Goerigk, Effect of the damping function in dispersion corrected density functional theory, *J. Comput. Chem.* 32(7), 1456 (2011)
33. D. Hobbs, G. Kresse, and J. Hafner, Fully unconstrained noncollinear magnetism within the projector augmented-wave method, *Phys. Rev. B* 62(17), 11556 (2000)
34. R. F. L. Evans, W. J. Fan, P. Chureemart, T. A. Ostler, M. O. A. Ellis, and R. W. Chantrell, Atomistic spin model simulations of magnetic nanomaterials, *J. Phys.: Condens. Matter* 26(10), 103202 (2014)
35. R. F. L. Evans, Vampire, VAMPIRE (2016), see: vampire.york.ac.uk/
36. G. Pizzi, V. Vitale, R. Arita, S. Blügel, F. Freimuth, G. Géranton, M. Gibertini, D. Gresch, C. Johnson, T. Koretsune, J. Ibañez-Azpiroz, H. Lee, J. M. Lihm, D. Marchand, A. Marrazzo, Y. Mokrousov, J. I. Mustafa, Y. Nohara, Y. Nomura, L. Paulatto, S. Poncé, T. Ponweiser, J. Qiao, F. Thöle, S. S. Tsirkin, M. Wierzbowska, N. Marzari, D. Vanderbilt, I. Souza, A. A. Mostofi, and J. R. Yates, Wannier90 as a community code: New features and applications, *J. Phys.: Condens. Matter* 32(16), 165902 (2020)
37. T. Chakraborty, K. Samanta, S. N. Guin, J. Noky, I. Robredo, S. Prasad, J. Kuebler, C. Shekhar, M. G. Vergniory, and C. Felser, Berry curvature induced anomalous Hall conductivity in the magnetic topological oxide double perovskite Sr_2FeMoO_6, *Phys. Rev. B* 106(15), 155141 (2022)
38. Y. Pu, D. Chiba, F. Matsukura, H. Ohno, and J. Shi, Mott relation for anomalous Hall and Nernst effects in $Ga_{1-x}Mn_xAs$ ferromagnetic semiconductors, *Phys. Rev. Lett.* 101(11), 117208 (2008)
39. C. Zeng, S. Nandy, and S. Tewari, Fundamental relations

for anomalous thermoelectric transport coefficients in the nonlinear regime, *Phys. Rev. Res.* 2(3), 032066 (2020)

40. A. Togo and I. Tanaka, First principles phonon calculations in materials science, *Scr. Mater.* 108, 1 (2015)
41. X. He, N. Helbig, M. J. Verstraete, and E. Bousquet, TB2J: A python package for computing magnetic interaction parameters, *Comput. Phys. Commun.* 264, 107938 (2021)
42. Q. Wang, Y. Xu, R. Lou, Z. Liu, M. Li, Y. Huang, D. Shen, H. Weng, S. Wang, and H. Lei, Large intrinsic anomalous Hall effect in half-metallic ferromagnet $Co_3Sn_2S_2$ with magnetic Weyl fermions, *Nat. Commun.* 9(1), 3681 (2018)
43. J. Xu, W. A. Phelan, and C. L. Chien, Large anomalous Nernst effect in a van der Waals ferromagnet Fe_3GeTe_2, *Nano Lett.* 19(11), 8250 (2019)
44. G. K. H. Madsen, J. Carrete, and M. J. Verstraete, BoltzTraP2, a program for interpolating band structures and calculating semi-classical transport coefficients, *Comput. Phys. Commun.* 231, 140 (2018)
45. N. Nagaosa, J. Sinova, S. Onoda, A. H. MacDonald, and N. P. Ong, Anomalous Hall effect, *Rev. Mod. Phys.* 82(2), 1539 (2010)
46. L. Xu, X. Li, X. Lu, C. Collignon, H. Fu, J. Koo, B. Fauqué, B. Yan, Z. Zhu, and K. Behnia, Finite-temperature violation of the anomalous transverse Wiedemann –Franz law, *Sci. Adv.* 6(17), eaaz3522 (2020)